Navier-Stokes Analysis for Engine Airframe Integration

E. Chaput, L. Barrera, C. Gacherieu, L. Tourrette
Aerodynamics Department
AEROSPATIALE - Aircraft Business
316 route de Bayonne F-31060 Toulouse Cedex 03

Abstract

The experience gained at Aerospatiale over the last two decades to overcome advanced experimental techniques and numerical methods for the design of engine-airframe integration, is now being strengthened by the industrial use of turbulent Navier-Stokes methods. The efficiency of this approach is demonstrated for the study of viscous effects around the pylon of a transonic aircraft. The separation of the boundary layers arises and disappears at the same flight conditions than observed in wind-tunnel simulations. The tricky problem of simulating the behaviour of the bleed system for the supersonic transport aircraft air-intakes is presented. The numerical difficulty lying in diminushing the influence of artificial dissipation with respect to physical one is pointed out in a comparison between Euler and Navier-Stokes analysis.

1. Introduction

Over the past twenty years, Aerospatiale has developed expertise on Engine Airframe Integration for both subsonic-transonic civil transport aircraft, with Airbus and ATR families, and supersonic aircraft with Concorde. Though experimental tools have largely contributed during this period to obtaining reliable results for engine airframe integration studies, it is currently accepted that for the design of any new transport aircraft the Computational Fluid Dynamics (CFD) tools have become reliable and robust enough to be used in complement of wind tunnel trials, reducing by the way the costs and cycle time for design. The computation of inviscid transonic and/or supersonic flows around complex full aircraft configurations can be carried out now by design engineers providing them with a very useful means for studying a large number of possible aerodynamic shapes before selecting a well optimised wind tunnel model.

In order to improve the design cycle even further it is important to have the capability of predicting almost all flow features which will be highlighted in the wind tunnel, including pressure induced separation on smooth surfaces, and shock induced separation of the boundary layer. The 3D turbulent Navier-Stokes codes capable of handling such complex configurations, exist in industry, but their level of robustness and the accuracy of their implemented turbulence models are still to be enhanced. This is presented in this paper by considering 2D and 3D complex configurations.

The first application considers the transonic flow around a full aircraft configuration. A multiblock mesh has been built around the AS28 wing-fuselage-pylon-nacelle configuration using about 3.5 millions mesh points. The choice of an algebraic turbulence model has been made for this case according to the lessons learned about simpler test cases, studying the sensitivity to the turbulence model of the viscous flow features suspected to arise close to the wing-pylon-nacelle interaction region. The comparisons of the results with respect to wind tunnel measurements are presented for cruise and low lift flight conditions respectively.

The second application deals with the improvement of the design cycle of supersonic air-intakes by using a turbulent Navier-Stokes code as an analysis tool. The aerodynamic performance of a supersonic aircraft power plant depends to a great extent on the inlet and moreover on the inlet bleed system design.

The gain provided by a Navier-Stokes analysis using a 2-equation turbulence model is demonstrated with respect to an Euler approach computing a generic 2D configuration defined at ONERA. A simple cavity located under the lower wall of a wind tunnel allows a secondary flow through a slot in the wall acting as a boundary-layer bleed to be obtained. Total pressure measurements performed downstream of the slot provide information on the distortion of the flow field within the diffuser.

Finally, a more realistic axisymmetric configuration with mixed compression air-intake is computed by the Navier-Stokes code to study the contribution of both numerical and physical diffusion terms to the capturing of the complex shock system taking place at Mach 1.9. The essential numerical difficulty lies for that case, in the modeling of the secondary flow, especially in the bleed cavity where viscosity plays a leading role.

2. Flow solvers

The same strategy was retained for both external and internal flows using a structured multiblock finite volume approach. The time-dependent 3D compressible Reynolds averaged Navier-Stokes equations in conservative form are integrated over the cells of a structured multiblock mesh. A cell-centered finite volume approach is used for spatial discretization of mean flow and turbulent transport equations. The viscous fluxes are calculated using the velocity and temperature gradients evaluated at the cell face center using the gradient theorem on a shifted control volume. The Sutherland's law is used for molecular viscosity.

For sub-transonic flows the NSMB code, initiated at EPFLausanne [1] and currently being developed in close co-operation between AEROSPATIALE, CERFACS, EPFL, KTH, and SAAB, is used in parallel mode on a CRAY-J916. This code is optimized for both parallel vector machine and super-scalar machine. The same version is used on a shared memory multi-processor and on the distributed memory of MPP machines. It can be run in serial or in parallel mode using message passing libraries .Both convective and viscous fluxes are computed using central differences with adaptive second and fourth order artificial dissipation terms. A diagonal alternating direction implicit algorithm is diagonalized at each point using a similarity transformation, following Chaussee and Pulliam [2]. This algorithm has been extended to solve the Navier-Stokes equations by adding the spectral radii of the viscous Jacobians to the inviscid implicit factors following Tysinger and Caughey[3]. Implicit boundary conditions have been developed which are consistent with both the characteristic theory and the physical boundary conditions.

For supersonic flows, the solver used in this paper, called FLU3M, was developped by ONERA in collaboration with Aerospatiale[4]. It solves Euler and turbulent Navier Stokes equations using an upwind scheme with MUSCL extrapolation [5] providing a second order accuracy in space with the assumption that mesh cells are evenly distributed and slightly distorded. The slopes inside each cell have to be limited to avoid any oscillations around discontinuities. This is obtained by using limiters, in order to satisfy Total Variation Diminishing (TVD) condition [6]. According to the choice of flux and limiter, the scheme contains more or less numerical viscosity. Roe's difference splitting flux [7] with Harten correction [8] and minmod limiter were employed for all viscous and inviscid computations below. The convergence of cavity computational zones in the following applications required to shift locally to a first order accuracy in space. A full ADI technique is applied for implicit time stepping, allowing the use of very large CFL numbers.

3 Transonic Engine Airframe Integration

The first application considers the transonic flow around a wing-fuselage-pylon-nacelle configuration for the study of the viscous effects on engine-airframe integration .

The optimisation of the pylon aerodynamics design is generally based on the minimization of the installation interference on lift and drag by building a pylon shape which allows the original pressure distribution of the isolated wing to be retrieved along the installed wing . In order to minimize the drag of the overall wing-pylon-nacelle configuration and supress possible induced vibrations it is then of the utmost importance to prevent any flow separation, in any of the cruise conditions.

Ten years ago, to study the aerodynamics of such complex configurations in details, Aerospatiale designed the AS28 half-model for wind-tunnel measurements. These experiments are now intensively used for CFD validation taking advantage of numerous pressure distributions along the wing, the pylon and the nacelle in both design and off-design conditions. Oil flow visualizations of the AS28G through-flow nacelle configuration are used in this paper to validate the computed viscous effects.

3.1 Turbulence Models[9]

An alternate model to the classical Baldwin-Lomax model (BL) when a flow separation due to an adverse pressure gradient is involved is the Granville (GR) algebraic turbulence model [10]. By assuming C_{cp} and C_{kleb} factors, being constants in the Baldwin-Lomax outer layer formulation, to be now functions of the modified Clauser pressure-gradient β, Granville imposes an outer similarity law with the outer formulation of the Cebeci-Smith model.

The implementation of the GR-model within the NSMB code takes into account the computational domain partitioning initially imposed by the multiblock mesh topology and arbitrarily modified for parallel computing efficiency. The following features are then required for an efficient use of the model for complex configurations of interest.

Despite the advantages described above the GR-model fails in many cases to predict large separation of turbulent boundary layers induced by a strong adverse pressure gradient. When such a separated flow appears about an airframe engine integration configuration, we have to study its sensitivity to the turbulence model. Then a model especially designed for this typical non-equilibrium flow like the Johnson-King (JK) model can be useful if it is implemented appropriately for complex configuration. The JK-model takes account of the convection and diffusion effects by solving an O.D.E. governing the streamwise development of the maximum shear stress derived from the turbulent kinetic energy equation using the Bradshaw relation between shear stress and turbulent kinetic energy. The 3D implementation of the model [11] within NSMB code benefits from the work already done for the generalisation of the GR-model.

3.2 Validation

The separation induced by a pressure gradient will be considered here in 2D at a rather low speed representative of take-off and landing regimes. The Aerospatiale A-Airfoil is a typical sudden stall airfoil which has been studied in detail at ONERA F1 and F2 wind-tunnels[12].

These experimental results constitute one of the most important data bases for Navier-Stokes codes and turbulence model validation, especially for the low-speed test case close to the stall at $M_\infty = 0.15$, $Re = 2.1\ 10^6$, $a = 13.3°$, since a trailing edge separation is highlighted by measurements which almost all classical turbulence models in use in industrial codes, fail to predict accurately. Moreover models insensitive to an adverse pressure gradient like κ–ε models do not predict any separation at all when algebraic models produce unphysical separation bubbles.

The computation was performed using a C-mesh including 148x64 cells assuming a $y^+ = 1$ at the center of the first cell above the airfoil. The transition from laminar to turbulent flow is imposed by setting $\mu_t = 0$ in laminar flow upstream of the observed locations in the experiments: x/c = 0.3 at pressure side and x/c=0.12 at suction side.

Figure 1 presents a comparison of how different turbulent models behave in that case by considering the profiles of the tangential component of the mean flow velocity at three stations downstream of the observed separation location in the experiments (two are normal to the airfoil surface at x/C=0.875 and 0.96, and one is normal to the free stream velocity at x/C =1.05 in the near wake). Where the experiments show a large separation bubble induced by a strong adverse pressure gradient, the BL-model, as expected , is insensitive to this gradient leading to a too large velocity at the trailing edge. The GR-model reduces the turbulent shear stress in the outer part of the boundary layer and of the wake, and shows that the velocity profiles are clearly influenced by pressure gradient but not enough to allow a good result on separated flow. This separation appears more physical when considering the JK-model in conjunction with the BL-model. Then the gain obtained by introducing the GR-model in the JK-formulation is still more impressive on velocity profile where only small discrepancies with respect to experiments remain on the outer part of the boundary layer.

The shock induced separation as a transonic effect has been studied [13] in 3D on a wing/body at cruise configuration, highlighting the interest of the GR-model which, in that case, provides similar accuracy as a two-layer κ–ε model does. Then for complex geometries like AS28G configuration a generalized implemention of an algebraic model accounting for pressure gradient was found a good choice providing the robustness and accuracy required for industrial applications.

3.3 Mesh generation

One of the key points for computing the airframe engine integration configuration is the mesh generation. A two-step procedure has been set up for building the mesh presented in figure 2. The first step makes use of ICEM-CFD tools for an Euler multiblock mesh. The second one is an orthogonalization-refinement step which allows the required number of points to be placed within the boundary layer. An in-house mesh genenator allows a Navier-Stokes mesh to be built automatically from an Euler one. The thickness of the boundary layer is defined by an analytical law based on the theoretical turbulent flow over a flat plate with the distance from the leading edge as a variable. The leading edge of the wing, the pylon and the nacelle for AS28G configuration are part of the topology of the multiblock mesh. An automatic procedure allows the mesh line from Euler mesh to become orthogonal to the aircraft surface before refining the mesh by adding nodes within the boundary layers. Then a structured multiblock Navier-Stokes mesh made of 62 blocks and 3.5 millions mesh points is obtained prescribing a y^+ value lower the than 1 at the center of the first cell (medium mesh) above solid surfaces and a number of nodes within the boundary layer ranging from 15 to 20 within the fine mesh.

Two additional levels of grid are extracted from this 'fine' mesh by taking every second point in each mesh direction in order to make a convergence strategy with grid-sequencing and/or multigrid possible.

3.4 Application to AS28G configuration

3.4.1 Wind tunnel test

AS28G is a generic 1/7.5 scale half-model which consists of a fuselage (6.4 m body length), a wing (3.704 m half-span with a leading edge fairing at the wing root), a pylon and a nacelle [14]. The motorization with a Turbo Powered Simulator (TPS) is not considered there. The measurements include chord-wise pressure distributions along 11 spanwise sections on the wing, ranging from η = 0.172 to η = 0.911 and colored oil flow pattern visualizations representative of the skin friction on the wing the pylon and the nacelle.

The test cases are defined as follows: M_∞ = 0.8, α = 2.2° (Case 1), α = 0.195° (Case 2), Re = 10.5 10^6 (based on aerodynamic mean chord C = 0.9408 m), transition being set at x/c =0.7 on the upper and lower surfaces of the wing, at x=0.075 m from leading edge on the nacelle and at x=0.035 m from the nose on the fuselage. The pylon is assumed to see a fully turbulent flow.

3.4.2 Computational Results

The computations have been performed with the parallel version of the NSMB code on a CRAY J916 using the GR-model as turbulent algebraic model. For the 3.5 millions points of the fine mesh a speedup of 6.4 was obtained on 8 processors leading to a performance of 467 MFlops.

Figure 3 illustrates the sensitivity of the pressure coefficient distribution to the size of the mesh by comparing at four spanwise stations (from η = 0.230 to η = 0.478, the pylon being positioned at η = 0.337) the computed solutions obtained for case 1 and case 2 configurations respectively on left and right hand side, using the medium and the fine mesh. The pressure side and the rear part of the suction side are well predicted, even for medium mesh using only 400000 mesh points. This very good agreement with measurements makes the demonstration that the aerodynamic load of the wing can be obtained by a Navier-Stokes approach even using a rather coarse mesh (i.e. at a low cost) where other viscous methods failed to predict this load correctly. The gain obtained when using the fine mesh is remarkable on the suction peak and on the position of the shock. Even though the shock seems to be well captured by the medium mesh, the fine mesh solution is more compatible with what it is expected when using the GR-model. That is to say downstream of the position observed in experiments. The Euler solution using 1.8 million points presented in the figure for case 1 allows us to understand the importance of viscous effects on that specific case.

In cruise condition (Case 1) the computed flow field is quite close to the observed flow in experiements. No separation was identified on the pylon. However in low lift condition (Case 2) a separation of the boundary layer appears at the junction of the pylon to the wing. The surface streamlines or skin friction lines (fig. 4) highlight the focus point of a three-dimensionnal separation. The surface streamlines from the attachment line at the leading edge of the pylon swirl around this point. The pylon flow then reattaches on the lower part of the wing following the black surface streamlines, where the flow from the wing leading edge attachment line is represented by grey surface streamlines. A secondary flow separation along the pylon wing junction is also well captured by the computation. These results are quite consistent with what is observed on wind-tunnel oil flow visualizations (fig. 4).

4. Supersonic inlet and bleed flow simulation

The function of a supersonic inlet is to slow down and compress the supersonic external flow to a subsonic flow on the engine face. This can usually be obtained by means of a supersonic compression, a strong compression through a normal terminal shock and a subsonic compression along the diffuser [15]. The inlet performance is characterized by the following parameters:

- the external drag depends on the internal cowl angle and can be reduced by the design of an internal compression intake.
- the pressure recovery η_f should be as high as possible. This can be obtained by both a proper choice of compression ramp angles and a low normal Mach number on the last supersonic compression. However, a low terminal normal Mach can induce the unstart phenomenon (internal compression inlets) or leads to high internal cowl angles (mixed compression inlets). In practice, the last normal Mach number is set around 1.30.
- distortion: the Mach number and total pressure distribution on the engine face have to be as homogeneous as possible. Unstart, subcritical and supercritical operations lead to an

increase in distortion, and can induce engine surging.

- stability margin: an adjustable inlet geometry is necessary to ensure the inlet operation at different values of free stream Mach. In practice, the regulation system in charge of adjusting geometry is not always quick enough to counterbalance both engine and external flow fluctuations. Inlet design is therefore performed for an operating point (given external flow and reduced engine mass flow), making sure that the inlet can bear previous fluctuations.

Bleed systems suck the boundary layer, and so improve distortion and pressure recovery by reduction of shock boundary layer interactions. They also act as an aerodynamic regulation system by bleeding extra mass flow caused by either an engine mass flow or free-stream Mach number drop. Finally, they change the shape of the engine characteristic operating curve, making the choice of an operating point with a higher value of pressure recovery possible. However, even if the bleed flow is ejected at the exhaust nozzle, it induces a thrust loss (or a bleed drag). Consequently, correct simulation of the bleed system is essential for the correct optimization of the engine airframe propelling balance.

Inlet operation is usually given by operating characteristics curves which represent mass flows and pressure recoveries of primary and secondary flow, for each engine operating point. Figure 5 shows the operating characteristic appearance of an internal compression inlet. Mass flow coefficients ε_t (total), ε_f (engine fan), ε_b (bleed) are calculated by the ratio of free streamtube sections and entry section A_e. The amount of bleed mass flow loss and the shape of the engine pressure recovery curve are closely linked to the bleed cavity response law. The bleed cavity response law is given by the secondary flow pressure recovery η_p for a given terminal shock position and Mach number condition above the cavity slot.

The present study deals with numerical simulation of the aerodynamic bleed system consisting of boundary layer bleeding through a slot located above a cavity. This secondary bleed flow is then evacuated in the ejector nozzle. The basic property of the secondary flow is the increase in its pressure recovery when the terminal shock moves upstream above the slot. Moreover, secondary mass flow is proportional to this pressure recovery. Thus, a reduction in engine mass flow induces an ascent of terminal shock and so an increase in secondary flow. As mentioned above, the bleed system plays the part of an aerodynamic regulation system. In the case of internal compression inlets, the increase in bleed mass flow is equivalent to a reduction in throat section delaying the unstart phenomenon.

A significant numerical difficulty in aerodynamic inlet simulation lies in the correct computation of the response law of this bleed cavity. Pressure recovery of secondary flow mainly results from viscous dissipation in the region of bleed jet entry and in the cavity recirculating zone. A correct evaluation of the secondary pressure recovery therefore depends on viscosity modeling in the cavity and bleed jet entry. The physical and numerical problem seems to be more difficult than the simulation of a separated flow past a backward-facing step.

4.1 Turbulence models

At first, turbulent Navier Stokes calculations were performed with the Baldwin Lomax model. The results were inadequate for a correct simulation of the cavity because all internal domains were laminar. The Baldwin Lomax model was only used in the computation of one operating point, in order to initialize k and ε values near walls. This initialization was obtained by an iterative process consisting in:

- defining free stream values k_∞ and ε_∞ for a given free stream turbulence rate and a given $(\mu/\mu_t)_\infty$ ratio .
- evaluating production rate P_k at each iterative step (function of k,ε and mean flow gradients) and set dissipation $D_k=\rho\varepsilon$ equal to P_k.
- evaluating k from Baldwin-Lomax eddy viscosity and previous ε : $\mu_t = f_\mu C_\mu k^2/\varepsilon = (\mu_t)_{B.L}$
- retaining maximum values between calculated and free stream ones.

The jet entry computational zone in the cavity was difficult to converge because of oscillations and high peaks in production rate P_k of turbulent kinetic energy. The convergence was obtained by limiting the ratio between production P_k and dissipation D_k [16].

Computations were performed on a Dec8640 machine (alpha processors, 300 MHz). The turbulent k-ε calculation time is about 250 microseconds per mesh cell and per iteration, and each operating point needs 3000-5000 iterations to converge.

4.2 Computational grids

The 2D meshes used for the following computations were built with the ICEM-CFD tool. About 15000 cells were necessary for Euler simulations and 75000 cells for Navier Stokes simulations.

The Euler mesh of supersonic inlet configuration is shown on figure 13. The geometries of both primary and secondary flows are extended by sonic throats in order to simulate the back pressure imposed by reduced engine mass flow and exhaust nozzle operating point. The outflow boundary condition becomes a supersonic one simpler than a prescribed pressure in a subsonic outflow. Then, different operating points creating operating characteristic curves correspond to different positions of terminal shock and are obtained by the variation of the primary throat size.

Navier Stokes meshes contain boundary layer domains close to the walls and following blunt leading edges and trailing edges. Figure 7 shows the detail of the mesh around the generic configuration bleed slot. Boundary layer domains usually contain about 35 cells normal to the wall and the size of first cell off the wall $y^+_{min} = y_1(\sqrt{\tau\rho/\mu})_w$ is taken to be around 0.25. This value is excessively small for the Baldwin Lomax zero equation model, but is required for the low Reynolds Jones-Launder k-ε two equation model.

4.3 Generic configuration

4.3.1 Experimental description [17]

This configuration was tested in ONERA S8Ch Chalais wind tunnel and consists of a cavity located under the lower wall of a wind tunnel. The wind tunnel section has an upstream sonic throat to fix entry mass flow and a downstream sonic throat to fix primary mass flow. Secondary flow is drained off through a secondary sonic throat (10.5% of entry section). Figure 6 shows the experimental geometry: total pressure measurements were performed downstream of the bleed slot, and upstream of the secondary sonic throat. Static pressures were measured on primary flow walls and cavity walls. Schlieren photographs and boundary layer probing on the lower surface upstream of the bleed slot are also available.

Wind tunnel dimensions at entry (after convergent duct) are 100 mm (height) x 120 mm (depth) and the Reynolds number based on the wind tunnel height is about $Re_h=1.25\ .10^6$. The Mach number above the bleed slot is around 1.30-1.35 which roughly corresponds to Mach number values in supersonic inlets throat region.

4.3.2 Results and Discussion

The calculated results were performed solving two-dimensional Euler and Navier Stokes equations at different operating points by varying primary throat height. Figure 8 compares shock patterns of the schlieren photograph and both inviscid and viscous computations for an intermediate shock position above the slot. Navier Stokes shock boundary layer interaction on the upper surface is closer to the schlieren photograph than the Euler solution. In the same way, the bleed jet entry aspect, near the downstream slot lip, is better predicted by viscous computation. In that case, experimental contact discontinuity coming from the upstream slot lip creates a λ shock due to the increase of cavity pressure. This phenomenon is also well simulated by inviscid computation and it creates a total pressure peak near the lower surface.

Figure 9 compares operating characteristic curves from experimental measurements, and inviscid and viscous computations. The primary pressure recovery η_f is a mean of experimental total pressure probing at station X=269.5. The primary operating characteristic curve (η_f function of ε_f) is thus very dependent on richness of experimental total pressure data. In that case, we have a good total pressure probing of near wall regions, so the Euler primary operating characteristic curve over-estimates pressure recoveries and the experimental one is better predicted by Navier Stokes computations.

Mass flow coefficients are evaluated with respect to entry mass flow. Consequently, secondary pressure recovery is a line, containing the point ($\varepsilon_f=1$, $\eta_p=0$) and having a slope proportional to secondary throat section. Therefore, it is quite normal that calculated points are roughly located on the same line. On the other hand, the variation range of η_p is more difficult to foresee. The comparison between experience, inviscid and viscous computations is not obvious: for the same shock position on the lower surface (above the slot), the shock position on the upper wall is significantly different between inviscid and viscous results (see figure 8). The first and last points of the operating curve roughly correspond to the same shock position on the lower surface. The viscous prediction of $\eta_{b\ max}$ is then closer to the experimental value.

Figure 10 shows static pressures on the upper surface for two operating points, corresponding to both an upstream and a downstream shock position on the lower surface. Upstream of the shock, there is a difference between experimental data and calculated pressures. Experimental pressure at the throat (X=0) is in good agreement with sonic state pressure, while the calculated sonic line seems to move forward in the upstream direction. The area around the throat section is very slightly evolutive

so the difference is probably due to side wall boundary layers which change aerodynamic throat position, not being taken into account by 2D computation. Consequently, computed boundary layer thickness at X=75mm is lower than the experimental value due to a higher external flow speed. Static pressures located downstream of the shock boundary layer interaction on the upper wall are in good agreement with experiments. The computed separation is slightly less severe than the experimental one but it is a well known behaviour of the Jones-Launder k-ε model [18-19]. Euler pressure profiles are shifted downstream due to the absence of boundary layer interaction (see figure 8).

Figure 11 shows total pressure distribution of the primary flow at station X=269.5 (downstream of the slot) corresponding to both a downstream and a middle shock position on the lower surface. Navier Stokes calculations can better simulate the total pressure peak caused by a λ-shock and the large total pressure loss near the upper wall which is typical of shock boundary layer interaction. The downstream position of the terminal shock is associated with the appearance of an expansion fan above the slot and thus a low value of total pressure near the lower surface. The discrepancy with respect to experimental values can be entirely explained by the difference on upstream Mach number. Experimental losses of total pressure near the lower surface are probably caused by a contamination of the upstream boundary layer which was not completely bled. This loss does not appear in the Navier Stokes computation because the upstream boundary layer thickness is smaller and bleed mass flow slightly higher than corresponding experimental ones. Inviscid and viscous total pressure profiles of the middle operating point have a peak near the lower surface, caused by interaction between shock and contact discontinuity coming from the upstream slot lip. The experimental profile does not have this peak because the bleed pressure is not high enough to create a λ shock by deflecting the contact discontinuity upwards.

4.4 Axisymmetric inlet configuration

4.4.1 Experimental description

Figure 12 shows a mixed compression axisymmetric inlet, tested by AEROSPATIALE in the Vernon LRBA wind tunnel. The secondary flow is drained off along a central core through a sonic throat of 7.9% of entry section. There are static pressure probes along along the internal cowl and central core walls. The total pressure probing at the diffuser exit is made up of 36 total pressure probes (6 radial x 6 circumferential). Radial distribution is poorer than the generic test, and the probes are situated outside the boundary layers. Consequently, the differences between Navier Stokes and Euler simulations are reduced when computational results are post processed in the same way as experimental data.

Free stream Mach number is 1.91 and Reynolds number based on entry radius is about $Re_r=2.39.10^6$.

4.4.2 Results and Discussion

Jones-Launder Turbulent Navier Stokes computations are performed at different operating points, making use of initial values coming from a Baldwin-Lomax computation at one operating point.

Figure 14 shows Mach number contours corresponding to supercritical and subcritical operating points . This configuration is an example of a mixed compression intake. In the supercritical operating case, supersonic compression finishes by a bow shock attached to the cowl lip. No strong shock boundary layer interaction arises because the flow becomes subsonic in the primary duct and the cowl lip shock does not interact with the ramp boundary layer. In that case, Navier Stokes results only differ from Euler ones close to the wall due to boundary layers. In the subcritical operating case, the cowl lip shock is detached and there is an interaction between the external shock and the ramp boundary layer. Total pressure losses caused by this interaction are not visible in diffuser total pressures so they were probably bled in the secondary flow.

Figure 15 shows the operating characteristic curves obtained from experiments, inviscid and viscous computations. The difference between inviscid and viscous is very small. The total mass flow of the viscous computation is slightly smaller than Euler one, because of the presence of boundary layers on conical ramps. Supercritical bleed flow (minimum value) is better predicted by Navier Stokes simulation, but then bleed pressure recoveries are very similar to Euler computations and slightly higher than experimental ones. However, it is important to note that the experimental geometry of the secondary flow duct differs from computational one by a longer and bent evacuation duct. This generates pressure losses which can explain the differences in secondary pressure recoveries.

Figure 16 shows total pressure profiles downstream of the bleed slot. The radial distribution of 6 experimental probes is illustrated

by arrows and experimental static pressure on the upper surface is added. Euler and Navier Stokes post processing of pressure recovery is made by the mean of set of the same six radial total pressures. The difference between viscous and inviscid calculations is located near walls, outside the experimental probes. It is the reason why primary pressure recoveries on operating curves are so similar between Navier Stokes and Euler computations. The subcritical operating point has a pressure loss caused by cowl shock detachment. Viscous and inviscid computations do not exactly corrrespond to the same operating point, but total pressure loss (down to static pressure at wall) is better predicted by viscous simulation.

Some numerical adjustments were applied in order to avoid any numerical problem and to ensure a good residue convergence history. The limitation of turbulent kinetic energy production rate is necessary in the jet entry zone and near the downstream leading edge lip, but it vanishes when convergence is reached. So, it does not disturb the final solution. On the other hand, inviscid and viscous computations were made with a first order space scheme in bleed cavity domains. The numerical viscosity is thus increased making analysis of the share between physical and numerical viscosity difficult.

The retained supersonic inlet configuration is one of the best ones predicted by Euler computations. The only shock boundary layer interaction is situated outside the inlet and so it does not basically change the inlet operation. On the other hand, internal compression inlets have shock boundary layer interactions inside the inlet which can induce unstarts not predicted by Euler computations [20].

5. Conclusion

The introduction of Navier-Stokes analysis for the design of engine-airframe integration has been undertaken at Aerospatiale for both sub-transonic and supersonic transport aircraft.

The accuracy and efficiency of the approach were demonstrated for the successfull study of viscous effects around the pylon of a transonic aircraft thanks to:

- an automatic mesh generation of boundary layers around complex geometries (up to 3.5 million points),
- an appropriate choice of turbulence models with respect to physic phenomena involved (flow separations),
- an efficient implementation of the method on parallel machines.

Its contribution to solve the tricky problem of simulating the behaviour of the bleed system for the supersonic transport aircraft air-intakes is presented with comparison with Euler approach. An appropriate limitation of the unphysical turbulent kinetic energy overproduction was applied making robust enough and accurate the κ–ε model implementation for the computation of complete operating characteristic curves by design engineers.

References

1 Vos J.B., Leyland P., Lindberg P.A., van Kemenade V., Gacherieu C. (1995) - "NSMB Handbook 3.3" , October 1995.

2 Chaussee D. S., Pulliam T. H., "Two-Dimensional Inlet Simulation using a Diagonal Implicit Algorithm", AIAA Journal, Vol. 19, Feb. 1981, pp. 153-159.

3 Tysinger T. L., Caughey D. A. , "Implicit Multigrid Algorithm for the Navier-Stokes Equations", AIAA paper 91-0242, 29th Aerospace Sciences Meeting, January 7-10, 1991, Reno, Nevada.

4 Cambier L., Darracq D., Gazaix M., Guillen Ph., Jouet Ch., Le Toullec L., "Améliorations récentes du code de calcul d'écoulement compressibles FLU3M", 77th AGARD Symposium on Progress and Challenges in CFD Methods and Algorithms, Seville, 1995.

5 Van Leer, B., "Towards the Ultimate Conserva-tive Difference Scheme V: A Second-Order Sequel to Godunov's method", Journal of Computational Physics, Vol 32, 1979, pp 101-136.

6 Harten, A., "High Resolution Scheme for the Computation of Weak Solutions of Hyperbolic Conservation Laws", Journal of Computational Physics, Vol 49, 1983, pp 357-393.

7 Roe, P.L., "Approximate Riemann Solvers, Parameters Vectors, and Difference Schemes", Journal of Computational Physics, Vol. 43, 1982, pp.357-372.

8 Harten, A. and Hyman, J.M., "Self Adjusting Methods for One Dimensionnal Hyperbolic Conservation Laws", Journal of Computational Physics, Vol. 50, 1983, pp. 235-269

9 Chaput E., Gacherieu C., Tourrette L - Workshop on Airframe Engine Integration, DLR, Braunschweig, pp. 7.1-7.12, March 1996.

10 Granville P.S. - "Baldwin-Lomax factors for Turbulent Boundary Layers in Pressure Gradients"
AIAA Journal, Vol. 25, pp. 1624-1627.

11 Abid R., Vatsa V.N., Johnson D.A., Wedan B.W. (1989), "Prediction of Separated Transonic Wing Flows with a Non-Equilibrium Algebraic Model", AIAA Paper 89-0558, 27th Aerospace Sciences Meeting, January , 1989, Reno, Nevada.

12 Gleyzes C.. (1989) - "Opération Décrochage - Résultats de la 2ème campagne d'essais à F2 - Mesures de pression et vélocimétrie laser", Rapport ONERA n° 0A 72/2259 AYD (CERT/DERAT n° 57/5004-22).

13 Tourrette L.., "Assessment of Turbulence Model for the transonic flow around the DLR-F4 Wing/body", AIAA

Paper 96-2034, 27th Fluid Dynamics Conference, June 1996, New-Orleans.

14 Becle J.P, "Essai de la demi-maquette AS28 dans la soufflerie S1Ma. - Partie Effets Reynolds et Partie TPS", Rapport d'Etudes ONERA n° 0962GY100G et 3423 AY043G, mai-juin 1985.

15 Seddon, J., Goldsmith E.L., "Intake Aerodynamics", Collins, London, 1985.

16 Menter, F. R., "Zonal Two Equation k-ω Turbulence Models for Aerodynamic Flows", AIAA Paper 93-2906, 24th Fluid Dynamics Conference, July 1993.

17 Barberis D., Corbel B., "Piège à couche limite pour entrée d'air supersonique. Etude du contrôle actif", Rapport technique ONERA n° 101/7078 AY, Décembre 1994.

18 Menter, F. R., "Two-Equation Eddy-Viscosity Turbulence Models for Engineering Applications", AIAA Journal, Vol. 32, No. 8, August 1994, pp. 1598-1605.

19 Leschziner, M. A., "EUROVAL - An European Initiative on Validation of CFD Codes", Results of the EC/BRITE-EURAM Project, 1990-1992, pp. 187-265 - Vieweg 1993.

20 Fujimoto, A., Niwa, N., Sawada K., "Numerical Investigation on Supersonic Inlet with Realistic Bleed and Bypass Systems", AIAA Paper 91-0127, 29th Aerospace Sciences Meeting, Reno, 1991.

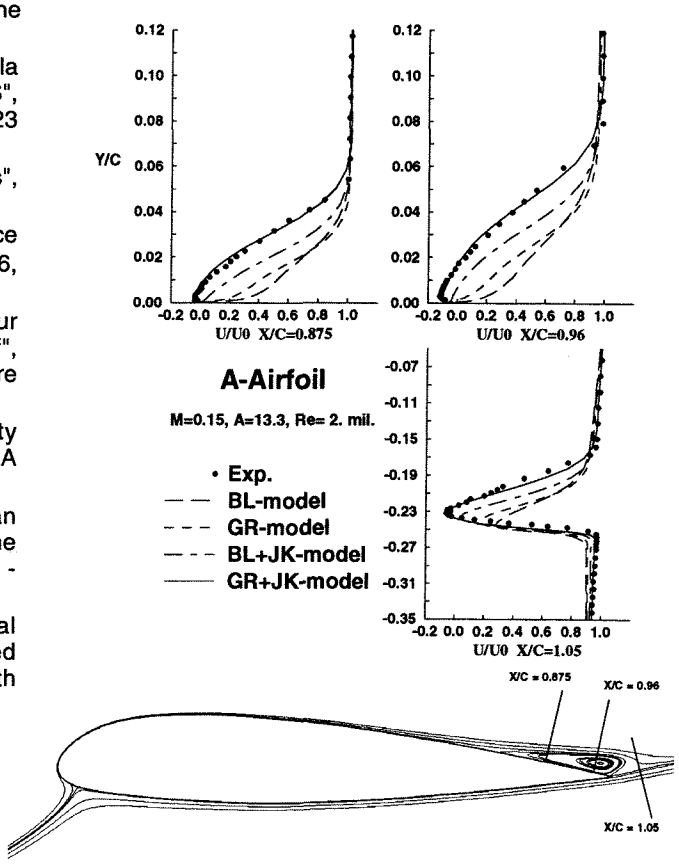

Figure 1 - A-Airfoil Velocity profiles in separated flow

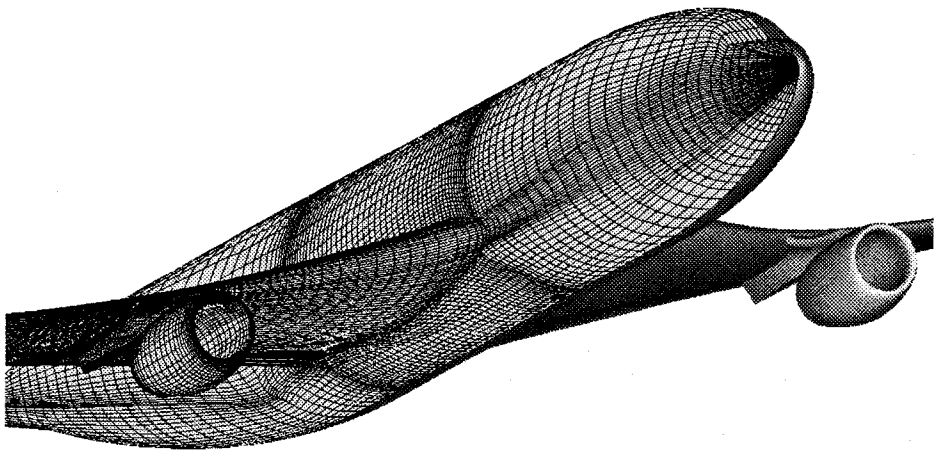

Figure 2 - Navier-Stokes mesh around AS28G model (3.5 million points)

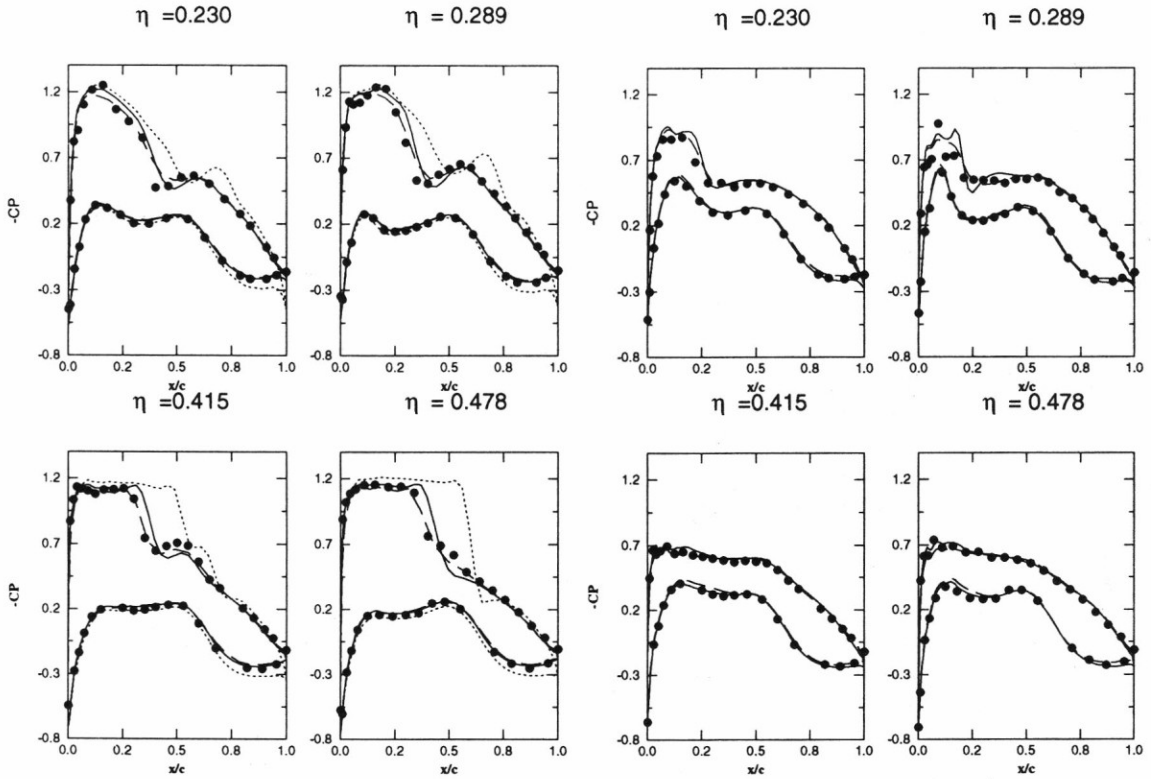

Figure 3 - $-C_p$ distribution at 4 spanwise sections of AS28G wing - Pylon at $\eta = 0.35$
• exp, ... Euler, - - - NS coarse mesh, _____ NS fine mesh
(Cz = 0.5 on left and Cz =0.27 on right)

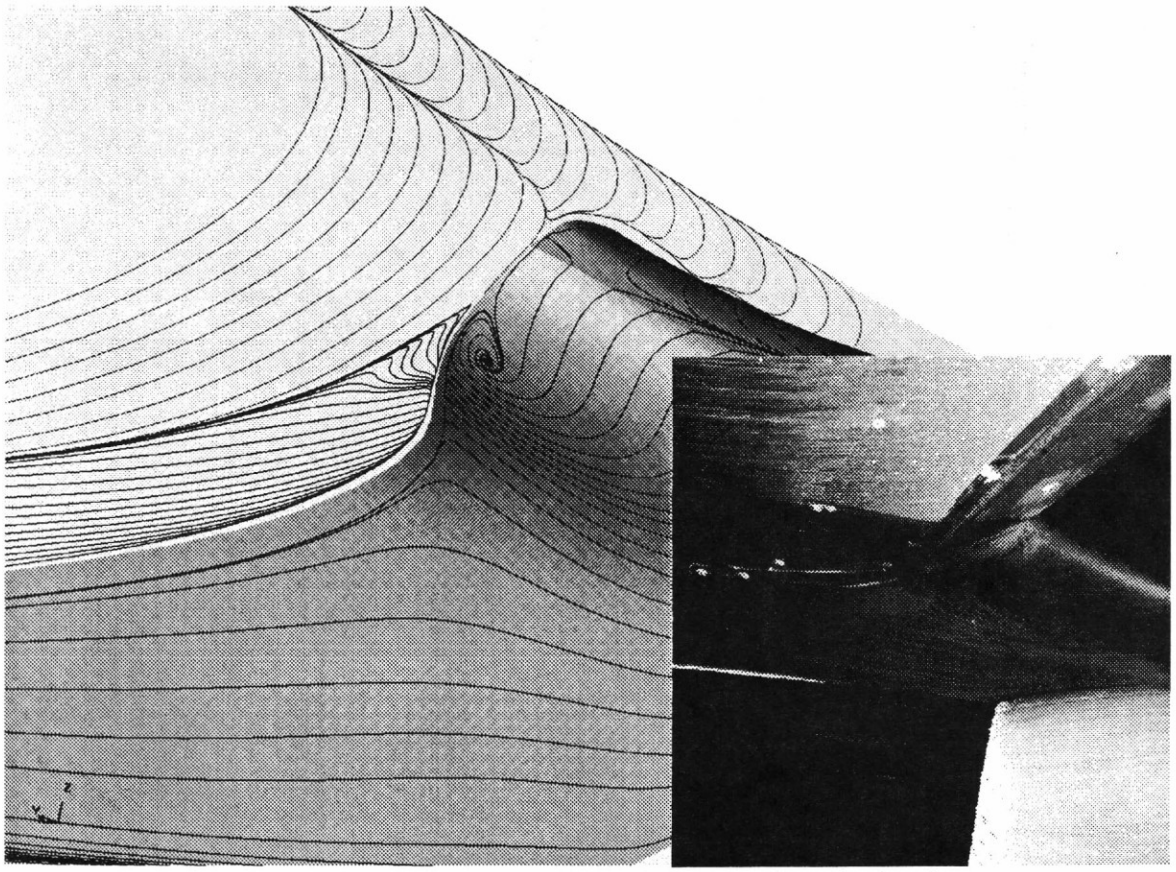

Figure 4 - AS28G (Cz = 0.27) - Skin friction lines at the wing pylon junction

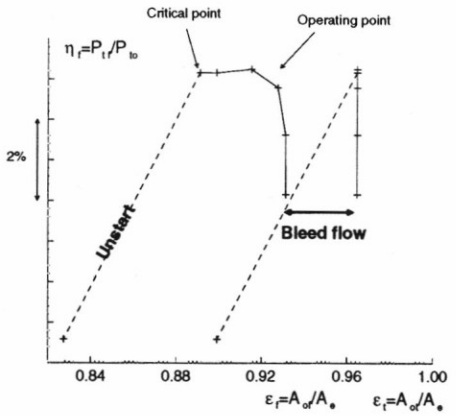

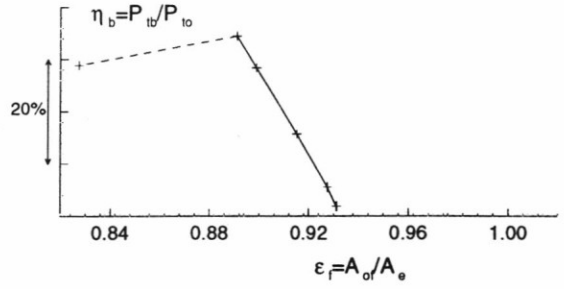

Figure 5. *Operating characteristic curves*

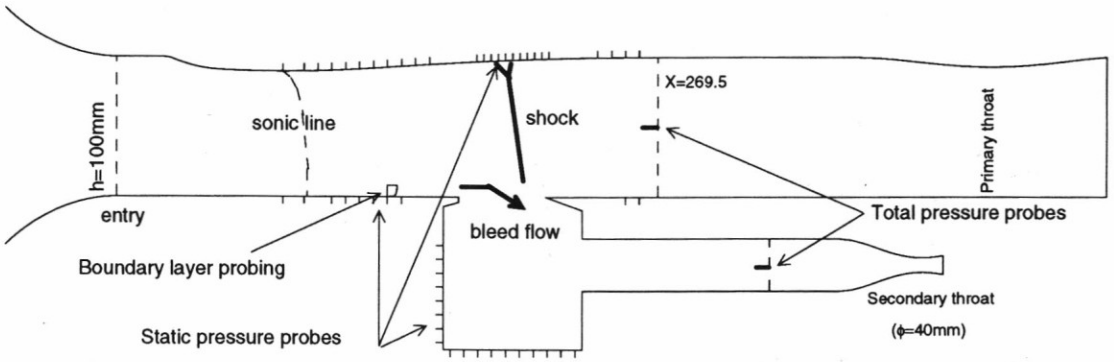

Figure 6. *Experimental description of generic configuration*

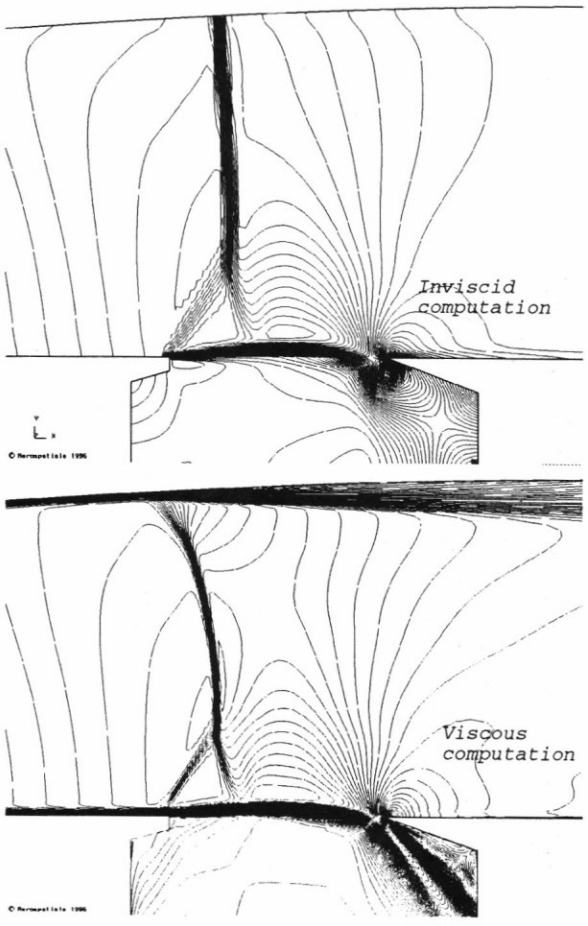

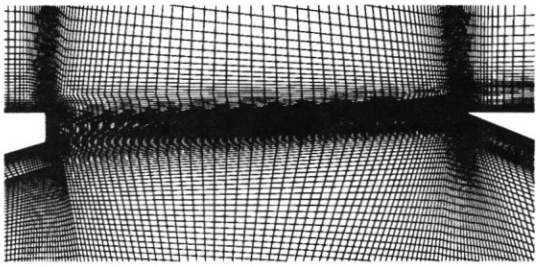

Figure 7. *Navier Stokes mesh at bleed slot of generic configuration*

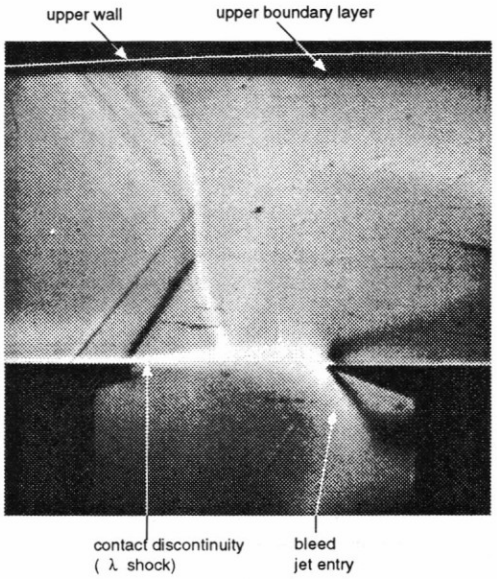

Figure 8. *Computed Mach number isolines and schlieren photograph (generic conf.)*

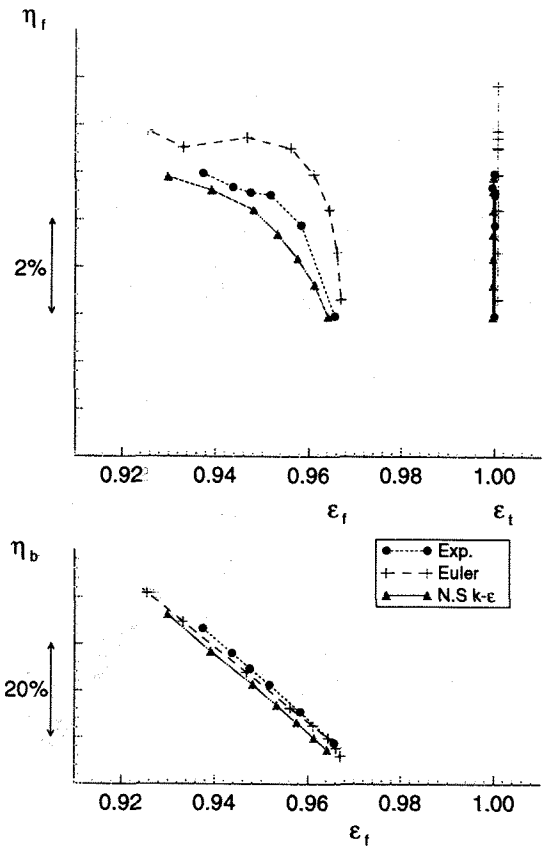

Figure 9. *Operating characteristic curves (Generic configuration)*

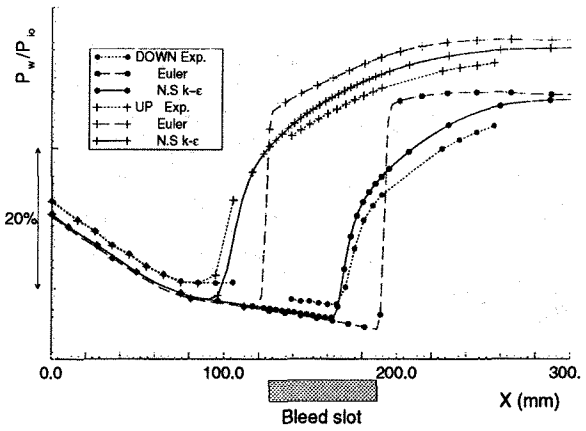

Figure 10. *Static pressure distribution on the upper wall (generic conf.)*

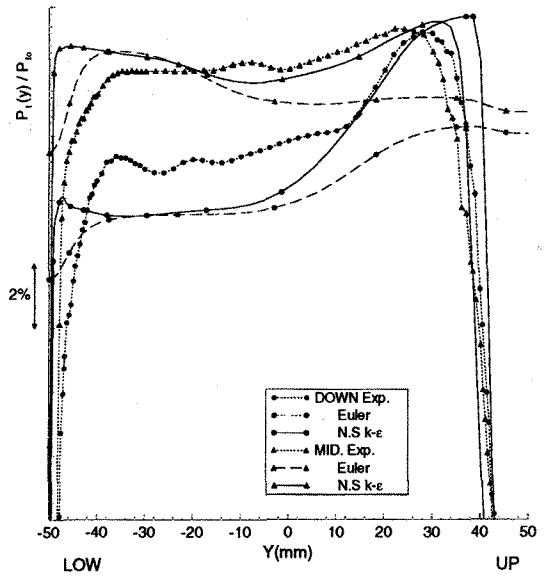

Figure 11. *Total pressure distribution at station X=269.5 (generic conf.)*

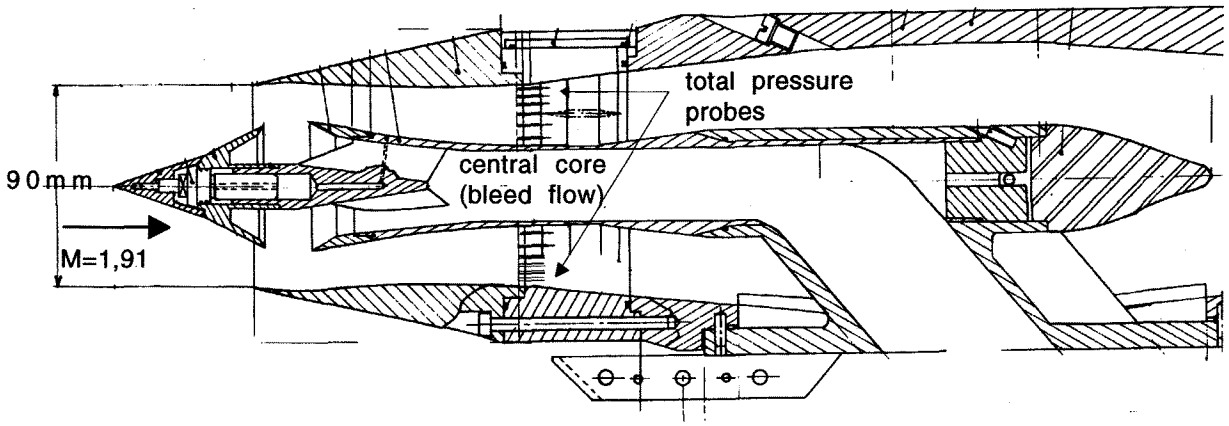

Figure 12. *External compression axisymetric inlet. Experimental description*

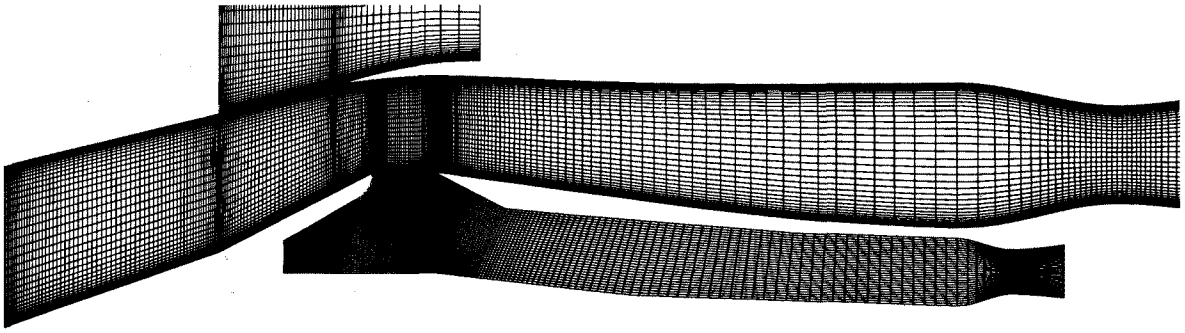

Figure 13. *Euler mesh of axisymetric inlet configuration*

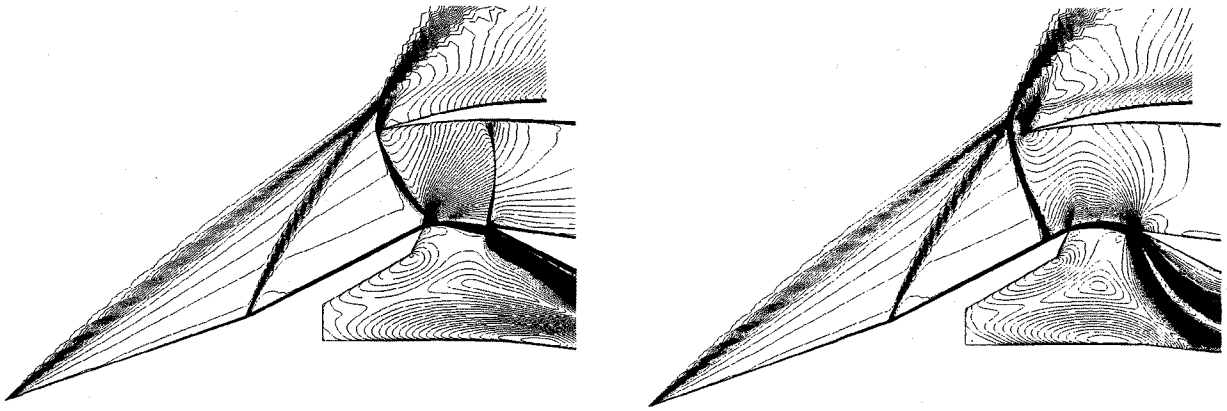

Figure 14. *Mach number isolines at supercritical and subcritical operating cases (viscous computation on axisymetric inlet)*

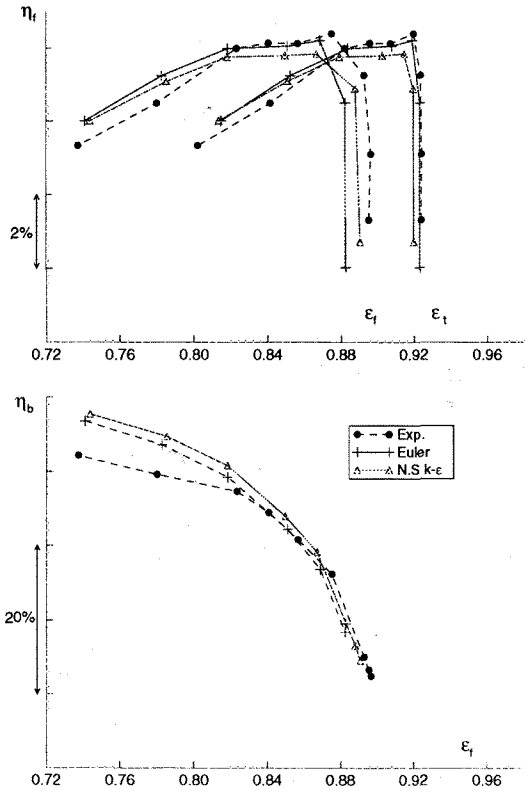

Figure 15. *Operating characteristic curves (axisymetric inlet configuration)*

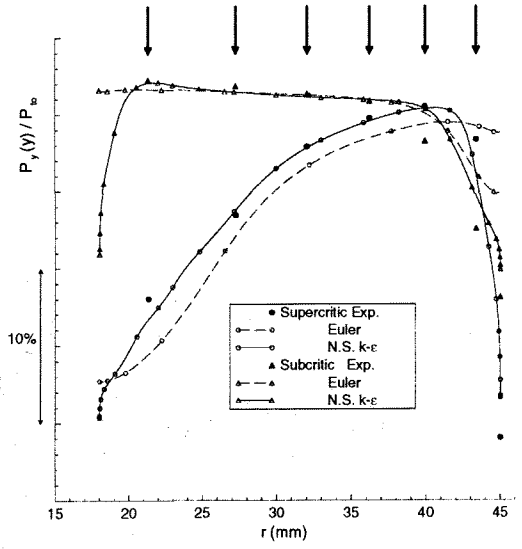

Figure 16. *Total pressure distribution in primary duct (axisymetric inlet configuration)*